Mechanochemistry for Energy Materials: Impact of High-Energy Milling on Chemical, Electric and Thermal Transport Properties of Chalcopyrite $CuFeS_2$ Nanoparticles

Peter Baláž,[a] Erika Dutková,*[a] Matej Baláž,[a] Róbert Džunda,[b] Jiří Navrátil,[c] Karel Knížek,[c] Petr Levinský,[c] and Jiří Hejtmánek[c]

Chalcopyrite $CuFeS_2$, a semiconductor with applications in chemical sector and energy conversion engineering, was synthetized in a planetary mill from elemental precursors. The synthesis is environmentally friendly, waste-free and inexpensive. The synthesized nano-powders were characterized by XRD, SEM, EDX, BET and UV/Vis techniques, tests of chemical reactivity and, namely, thermoelectric performance of sintered ceramics followed. The crystallite size of ~13 nm and the strain of ~17 were calculated for $CuFeS_2$ powders milled for 60, 120, 180 and 240 min, respectively. The evolution of characteristic band gaps, *Eg*, and the rate constant of leaching, *k*, of nano-powders are corroborated by the universal evolution of the parameter S_{BET}/X (S_{BET}-specific surface area, *X*-crystallinity) introduced for complex characterization of mechanochemically activated solids in various fields such as chemical engineering and/or energy conversion. The focus on non-doped semiconducting $CuFeS_2$ enabled to assess the role of impurities, which critically and often negatively influence the thermoelectric properties.

1. Introduction

Chalcopyrite $CuFeS_2$ composed of earth-abundant, non-toxic and inexpensive elements is a mineral with tetrahedral structure. The structure can be considered as a double-sfalerite cell in which two Zn atoms are replaced orderly by one Cu ion and one Fe ion. This ordered arrangement in the lattice is in tetrahedral coordination with sulfur. The lattice constants of the tetragonal cell are a = 5.291 Å, c = 10.422 Å.[1] CuS_4 and FeS_4 tetrahedra are connected in a corner – sharing manner.[2] The sulfur atom displaces from the center of the bonded tetrahedron, arising that the Fe–S bond is stronger and more anisotropic than the Cu–S bond.[3]

$CuFeS_2$ is known to be an antiferromagnetic semiconductor at ambient pressure. The majority of its carriers are of p- or n-type depending on sample.[2c,4] Its interesting semiconductor properties favor research into its thermoelectric performance.[5] Research encompasses synthetic as well as natural species.[6] To improve its thermoelectric performance the doping is frequently applied to enhance the carrier concentration and electrical conductivity.[3,7] Next to the doping, also nanostructuring plays important role to improve transport properties in thermoelectric materials.[8] Creation of solid state defects in form of multinary boundaries and interphases leads to the phonon scattering and reduction of thermal conductivity which enhances TP.[9] This concept was also verified for $CuFeS_2$.[7d,10]

Mechanochemistry is now regularly applied to produce nanostructures useful in various fields.[11] The high-energy ball milling was also accepted in thermoelectrics among the non-equilibrium recipes like melt-spinning and self-sustaining heating synthesis to prepare multiscale nanostructures and /or to synthesize nanosized thermoelectrics.[12]

Recently several papers were published by our research group aimed at elucidation of thermoelectric performance of mechanochemically treated chalcopyrite $CuFeS_2$. Research into its synthesis,[13] intrinsically doped samples,[14] combination of natural and synthetic chalcopyrites[6b] as well as the scaling possibility[15] opened new roads for further research into this promising semiconductor. The results were challenging, however a systematic study of prolonged milling of synthesized chalcopyrite was not performed up-till now. Therefore, the aim of this paper is to elucidate impact of high-energy milling of $CuFeS_2$ nanoparticles on its physicochemical properties, especially on transport properties. For this study we have chosen the "pure" undoped semiconducting $CuFeS_2$. The straightforward reason consists in the much higher sensitivity of the undoped $CuFeS_2$ to probe the role of "impurity phases", e.g. digenite $Cu_{1.8}S$, pyrhotite Fe_7S_8, or other electrically conducting phases which influence the electric and thermal transport of resulting sulfides due to the percolative nature of electrical transport. As a result, these parasitic phases can essentially influence the thermoelectric performance of the material being "hidden" for XRD and EPMA analysis due to their low

[a] Prof. P. Baláž, Dr. E. Dutková, Dr. M. Baláž
Institute of Geotechnics, Slovak Academy of Sciences
Watsonova 45, 04001 Košice, Slovakia
E-mail: dutkova@saske.sk
[b] Dr. R. Džunda
Institute of Materials Research, Slovak Academy of Sciences
Watsonova 47, 04001 Košice, Slovakia
[c] Dr. J. Navrátil, Dr. K. Knížek, Dr. P. Levinský, Dr. J. Hejtmánek
Institute of Physics of the Czech Academy of Sciences
Cukrovarnická 10, 16200 Prague, Czech Republic

concentration, poor crystallinity, small size etc. The presence of such "low concentration" parasitic phases is undiscoverable in optimally doped chalcopyrite which, due to the "robust" adjustment of its electric transport properties to degenerate limit, does not enable to unmask the role of impurities.

2. Results and Discussion

2.1. Bulk and Surface Characterization

In Figure 1 XRD patterns of the synthetized $CuFeS_2$ samples are shown (B–E). For comparison the pattern of non-milled natural $CuFeS_2$ is also shown (A). The peaks are indexed to the tetragonal $CuFeS_2$ (JCPDS 01-075-6866). The intensity of peaks for milled samples broaden and declines. Some adjacent peaks overlap, namely 204/220 and 312/116. It reflects the changes in lattice strain and crystallinity degree.[16] In non-milled natural sample (A) also admixtures of quartz SiO_2 and siderite $FeCO_3$ from mineral deposit are shown. In milled samples (B–E) pyrite FeS_2 as an admixture created during the synthesis is present. Closer examination of sample milled for 60 min (B) was performed by Mössbauer spectroscopy in our previous work.[6b] The patterns of milled samples show broad peaks which reflect nanocrystalline and disordered structure of $CuFeS_2$. The Rietveld refinement was used to estimate the crystallite size and strain of the particles. The crystallite sizes of 13, 9, 14 and 13 nm and the strain 16, 14, 17 and 22 were calculated for $CuFeS_2$ treated for 60, 120, 180 and 240 min, respectively. It follows that the crystallite size reaches its saturation value around 12 nm. Both the size reduction down to the nanometer scale as well as simultaneous increase of lattice disorder as a consequence of induced strain have positive effect on thermoelectric performance. Effect of nanostructuration leads to the formation of a large number of grain boundaries which serve as phonon scattering centers and consequently to reduction of lattice thermal conductivity.[8e]

Values of specific surface area, S_{BET} (1), crystallinity, X (2) and band gap, E_g (3) in dependence on milling time, t_M of $CuFeS_2$ are given in Figure 2. Surface area, S_{BET} of milled samples (curve 1) sharply increase till $t_M = 120$ min. However, this increase is slowing at higher milling times and even at 240 min the decrease of S_{BET} values is observed. At the beginning of milling the small particles are generated resulting in an increase of S_{BET}. Later on, further comminution is reduced, or there may be even an increase of particle size due to the interaction of fines. This effect is characterized by agglomeration of particles as a consequence of van der Waals forces and/or chemical bonds.[17] Accordingly, the adequate morphology of $CuFeS_2$ particles can be observed, see Figure 5. As a whole, changes in specific surface area are source of two-dimensional defects (surface defects) where the periodicity of the structure is disturbed or interrupted.[18]

Crystallinity, X of milled samples (curve 2), as an integral characteristic of bulk defects, shows an opposite tendency. The calculated values are very low and close to each other (X = 22–29 %) in whole milling interval 60–240 min. Corresponding XRD patterns are in Figure 1. The levelling of X values corresponds to the same tendency in values of crystallite sizes and strain, see previous paragraph. It is known in mechanochemistry that during mechanical activation the size of crystals decreases to some critical values.[11a] As stated in,[19] prolonged energy supply by high-energy milling causes progressive deformation of the crystals and energy accumulation in their volume or at the surface. In our case, the population of bulk defects represented by X values is not so broad as in case of surface defects represented by S_{BET} values. As an example, let us compare samples milled for 60 and 120 min, respectively. While S_{BET} values increased from 2.5 $m^2 g^{-1}$ to 4.4 $m^2 g^{-1}$, i.e. 1.8 times, X values decreased from 29 % to 27 %, i.e. only 1.1 times. It follows that by mechanical activation of chalcopyrite $CuFeS_2$ the population of surface defects is more developed in comparison with bulk defects.

The concept of effective surface area as an integral character of surface defects for evaluation its influence on reactivity of mechanically activated solids was introduced.[20] Later a concept to unify surface and bulk changes generated during mechanical activation into a joint parameter was

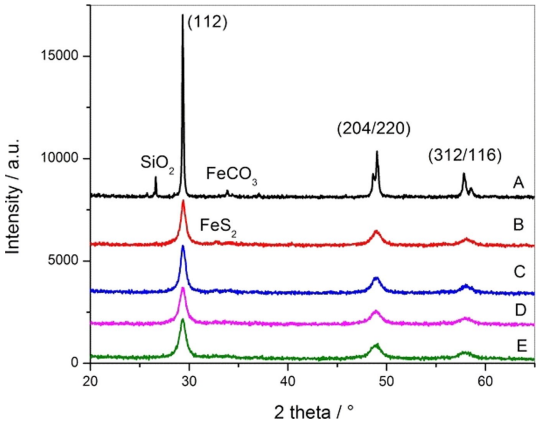

Figure 1. Powder X-ray diffraction patterns (XRD) of chalcopyrite $CuFeS_2$. Milling time: A) 0 min (standard, natural mineral), B) 60 min, C) 120 min, D) 180 min, E) 240 min.

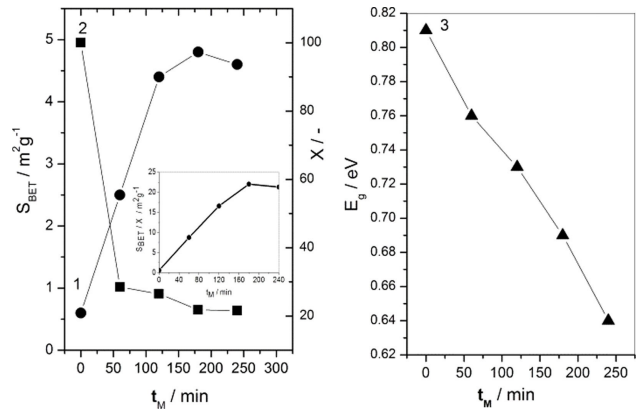

Figure 2. The influence of milling time, t_M on specific surface area, S_{BET} (1), crystallinity, X (2) and band gap, E_g (3) and for chalcopyrite $CuFeS_2$ (in Inset dependence of S_{BET}/X on milling time t_M is given).

elaborated by introducing the structure imperfections in solids.[21]

This parameter defined as S_{BET}/X was applied in[22] for evaluation of solid state reactions influenced by mechanical activation. This parameter was used also in our study to verify its applicability for characterization of semiconductor properties, see the following paragraph. Its dependence on energy supply to $CuFeS_2$ by milling is shown in inset of Figure 2. The straight line was obtained for all milled samples except of the one milled at 240 min. Here, the decrease in S_{BET} value influenced the straight line tendency.

In Figure 3 UV/Vis absorption spectra of chalcopyrite $CuFeS_2$ treated for different milling times are shown. Based on Tauc plots (see Inset) the values of energy bandgap E_g for individual samples of chalcopyrite were determined. Accordingly, there is an unambiguous tendency of E_g decrease with increasing supply of energy by milling.

2.2. Structure Sensitivity of Band Gap

In semiconductor science manipulation with energy band gap E_g can influence the thermoelectric performance of a material.[23] Usually, higher electrical conductivity can be overcome by using semiconductor with lower value of E_g and/or by application of the dopant. The tendency of lowering E_g values was observed also in our study. In Figure 4a dependence of E_g values on parameter S_{BET}/X for mechanically activated chalcopyrite $CuFeS_2$ is shown. From a given linear plot the structural sensitivity of bandgap energy E_g can be identified. However, in the region with S_{BET}/X values higher than 21 $m^2 g^{-1}$ the plot is changing and does not fit into this trend. Explanation can be found in Figure 2, where for milling time 240 min a decrease in value of specific surface area S_{BET} can be observed. This is connected with particle interaction (agglomeration) where smaller particles created by high energy milling are joining into larger ones.[17] More intimate contact in polydispersed particles has impact on changes of ultrafine structure of chalcopyrite grains with consequences on its electronic properties. However, this phenomenon is not harmful for further E_g decrease as can be observed in Figure 4. It follows that for a decrease of E_g the bulk disordering of $CuFeS_2$ (manifested by decrease of the crystallinity degree X) is more decisive than its surface disordering (manifested by increase of specific surface area S_{BET}).

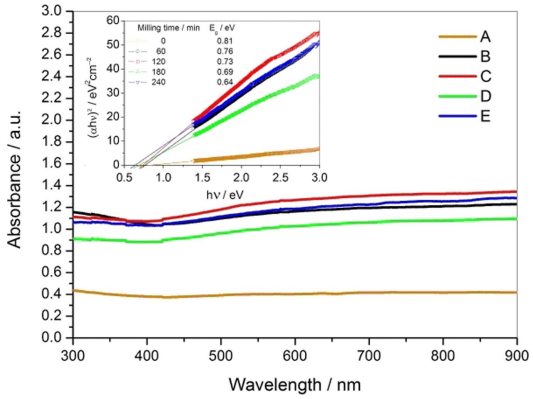

Figure 3. UV/Vis spectra of chalcopyrite $CuFeS_2$. Milling time: A) 0 min, B) 60 min, C) 120 min, D) 180 min, E) 240 min (in Inset Tauc plots are given).

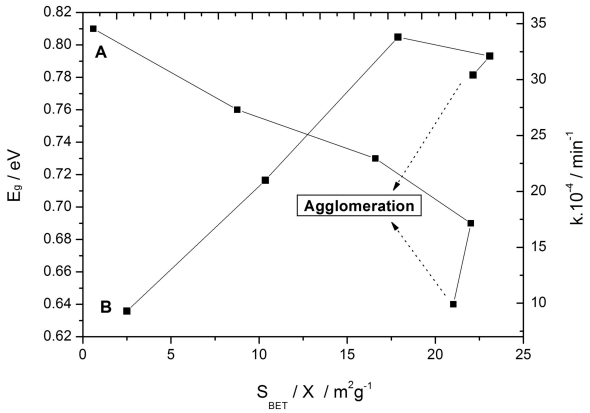

Figure 4. Energy band gaps, E_g (A) and rate constants, k (B) vs. S_{BET}/X for chalcopyrite $CuFeS_2$ milled for 0–240 min.

2.3. Morphological Characterization

Scanning electron micrographs (SEM) of chalcopyrite milled for different times are given in Figure 5. For comparison, SEM of standard (non-activated) $CuFeS_2$ is shown in Figure 5a. In this case typical large chalcopyrite grains in combination with smaller ones can be detected. The poly-dispersive character of

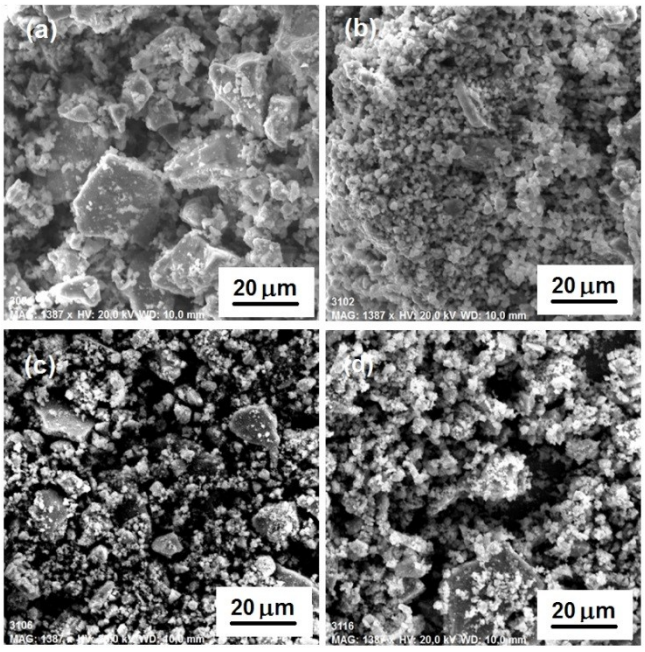

Figure 5. Scanning electron micrographs (SEM) of chalcopyrite $CuFeS_2$, milling time: a) 0 min (standard, natural mineral), b) 60 min, c) 120 min, d) 240 min.

the grains is a consequence of applied dry sieving procedure in which the sieve with mesh less than 35 μm was used. In Figure 5b the grains of synthesized $CuFeS_2$ by milling for 60 min are shown. Next to the large micrometer grains also the very small grains showing occurrence the possible nanometer size can be detected. The occurrence of large grains can be a consequence of brittle-ductile transformation in mechanically activated $CuFeS_2$ where plastic deformation instead of fracture occurs.[16a] Again, the sample is poly-dispersive in its morphology. Trend to formation of smaller grains is further manifested in Figure 5c where their population is prevailing. This is in accord with the large S_{BET} value for this sample milled for 120 min (see Figure 3). Finally, at milling time 240 min the population of smaller grains is again present (Figure 5d). The small grains have tendency to agglomerate into the larger ones (nanocomposites) which corresponds with the decrease of S_{BET} values in Figure 3. Nanocomposites retain a size in a nanometer range (see discussion around Figure 1) and can be responsible for the decrease in a thermal conductivity because they serve as phonon scattering centers.[12] Poly-dispersive character of products can be also beneficial for thermoelectric performance. As stated in[24] these multiscale distributions positively influence phonon scattering.

2.4. Chemical Reactivity

In Figure 6 dependence of Cu and Fe dissolution from mechanically activated chalcopyrite $CuFeS_2$ is shown for samples treated for different milling time. In order to identify differences between Cu and Fe dissolution, the ratio of dissolved metals Cu/Fe was applied. For comparison, the results for standard (non-milled) chalcopyrite are also presented. According to equation (2), both metals are dissolved as soluble chlorides and their molar ratio in solution has to be equal. 1. However, the experimental data are different. It follows from the presented plots that there is a dependence of Cu/Fe ratio on leaching time. Value Cu/Fe = 1 was reached only for standard (non-milled) sample at $t_L \geq 15$ min. However, a tendency to reach this equilibrium value is manifested also for the milled samples. Moreover, the course of metals dissolution varies with milling time t_M. In order to clarify this sensitivity, the rate constants, k were calculated from the linear parts of Cu/Fe dependence vs. t_L in the interval $t_L = 15$–60 min (Table 1). Selection of the linear interval was based on inspection of the leaching curves in Figure 6. At the beginning ($t_L < 15$ min), the dissolution is very fast. We interpret this phenomenon as a consequence of possible presence of Cu^{2+} and Fe^{3+} soluble sulfates on surface of nanocrystalline chalcopyrites.[25]

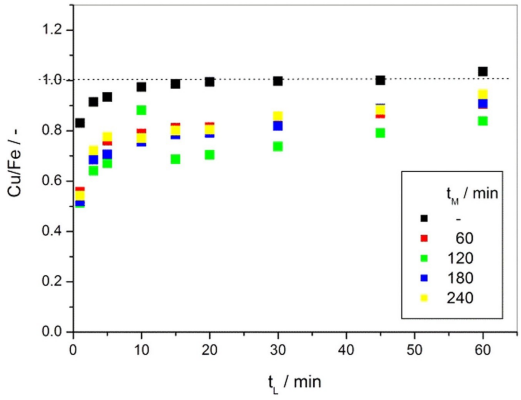

Figure 6. The leaching of copper and iron (defined as Cu/Fe ratio) from chalcopyrite $CuFeS_2$ milled for different times, t_M – milling time, t_L – leaching time.

To verify the structure sensitivity of reaction (2), the calculated rate constants of leaching, k vs. S_{BET}/X values are given in Figure 4 (plot B), where the same dependence is shown for E_g. Again, the structure sensitivity of leaching is documented as in case of energy band gap E_g, Figure 4 (plot A). The both plots refer on the potential universality of parameter S_{BET}/X for characterization of disordered solids in such diverse fields as chemical engineering and/or semiconductor physics.

This structure sensitivity of leaching must be consequence of changes in disordered structure of chalcopyrite. It follows from the leaching curves in Figure 6 that the Cu/Fe ratio is always lower than 1 for all mechanically activated samples. It means that Cu is dissolving slower in comparison with Fe. However, with increase of chemical impact (time of leaching) and/or mechanical impact (time of mechanical activation) there is a trend to level of these differences. Explanation can be related to the structural changes of chalcopyrite because of mechanical activation. To help in elucidation of solid-state changes in $CuFeS_2$, EDX analysis of the powdered samples was performed (Table 1). EDX method has penetration depth ~150 nm[7h] and can provide the average content of elements in bulk of the synthesized species for which the average crystallite size ~12 nm was determined by XRD in our case. The EDX data for copper and iron content in solid phase show some variation of the values. Cu is enriched for samples milled for 120–240 min. However, content of Fe is relatively stable and not different in comparison with the standard (non-milled) sample. The only compelling ascertainment is sulfur content which decreases with the milling time. Liberation of sulfur from $CuFeS_2$ due to the high-energy milling was already proved for natural mineral.[25b,26] Tetragonal low-temperature modification $CuFeS_2$ (α-phase) is transformed to the high-temperature modification $CuFeS_{2-x}$ (β-phase) which is sulfur deficient. According to[25b] where β-phase was obtained by syntheses with variation of sulfur content, the value x = 0.25. However, their results were not normalized. In our case, EDS results for t_M =

Table 1. The rate constants of leaching, k and EDX analysis of chalcopyrite $CuFeS_2$ in dependence on milling time, t_M.

Milling time t_M/min	Leaching k. 10^{-4}/min^{-1}	R^2	EDX analysis (not normalized)
0	9.3	0.82174	$Cu_{1.04}Fe_{1.07}S_{1.89}$
60	21.0	0.96564	$Cu_{1.03}Fe_{1.08}S_{1.89}$
120	33.8	0.99947	$Cu_{1.11}Fe_{1.06}S_{1.83}$
180	30.4	0.96852	$Cu_{1.10}Fe_{1.08}S_{1.82}$
240	32.1	0.97411	$Cu_{1.11}Fe_{1.11}S_{1.78}$

240 min were re-calculated and the normalized composition $Cu_{1.00}Fe_{1.00}S_{1.60}$ was obtained. The sulfur liberation during milling leads to the rupture of chemical bonds where sulfur is involved and subsequently to the reconstruction of chalcopyrite structure. Here Cu–S and Fe–S bonds are destabilized according to their length and strength. Bond distances in non-treated tetrahedral $CuFeS_2$ are 2.272 Å and 2.287 Å for Cu–S and Fe–S, respectively.[2a] Fe–S bond is stronger and more anisotropic than the Cu–S bond.[3] In our case, a selective increase of Cu dissolution with milling time is observed. According to[27] the selective influence upon one part of the crystal lattice is a characteristic feature of solids with closed-packed structural units. Mechanical impact may lead to the delocalization of copper ions which in its sublattice manifest as a liquid-like state beneficial for chemical leaching[28] as well as for lowering of thermal conductivity.[2b,8f]

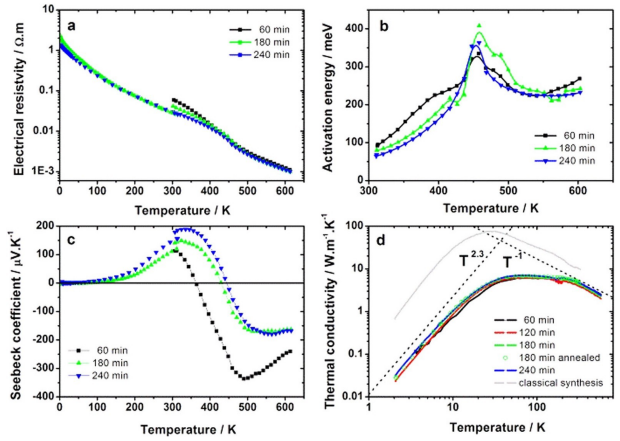

Figure 7. Thermoelectric properties of sintered and annealed samples of chalcopyrite $CuFeS_2$ as a function of temperature. a) electrical resistivity, b) activation energy, c) Seebeck coefficient, d) thermal conductivity (in Figure 7D the gray curve contrasts the thermal conductivity of the milled nano-grained samples to a "classically" synthesized chalcopyrite[29] with relatively large grains).

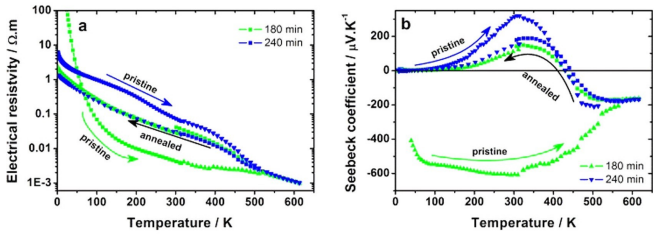

Figure 8. Thermoelectric properties of sintered samples as a function of temperature showing the effect of annealing. a) electrical resistivity, b) Seebeck coefficient.

2.5. Thermoelectric Properties

The study of the duration of high-energy milling procedure in connection to the thermoelectric properties was performed using "pure" undoped initial composition of $CuFeS_2$. We remember the idea to employ the semiconducting nature of pure $CuFeS_2$ which offers, due to the highest sensitivity of "utmost" insulating matrix, to "unveil" the role of impurities on both electrical and thermal transport. The "standard" approach based on maximizing Figure of merit *ZT* would not enable such study. Temperature dependence of the thermoelectric properties of the samples is shown in Figure 7 and 8. While measurements of the electrical resistivity ρ and Seebeck coefficient *S* upon cooling below room temperature were completely reproducible, heating cycles above room temperature up to 600 K led to irreversible changes in both ρ and *S*. On the other hand, this was not the case for the thermal conductivity κ which was unaffected by high temperatures. Most importantly, due to the high temperature thermal cycling between 300 and 600 K, ρ and *S* stabilized and could be measured reproducibly. Figure 7 shows data for such "annealed" samples. Figure 8 shows how ρ and *S* evolved from "pristine" to "annealed" samples. This behavior is depicted in Figure 7a and 7c as follows: opaque curves below 300 K represent the properties of pristine samples, semi-transparent curves above 300 K show how the properties evolved upon heating and finally, opaque curves above 300 K show the reproducible properties after thermal cycling. Furthermore, low temperature data of one sample after thermal cycling are also displayed; another sample showed the same behavior after thermal cycling but we omitted the data to maintain clarity of the graphs.

$CuFeS_2$ is a semiconductor and as such, its resistivity and Seebeck coefficient may be used as a probe into the phase purity of the samples. Of all the samples, only the behavior of the one milled for 180 min closely resembles that of a "typical" low-doped $CuFeS_2$ below 300 K – that is (see Figure 8), its resistivity increases sharply with decreasing temperature to surpass 100 Ω m and its Seebeck coefficient is negative with an absolute value of several hundred $\mu V\,K^{-1}$ and without significant dependence on temperature above 100 K.[29]

On the other hand, the other samples (as well as the 180 min sample after thermal cycling) display a different behavior when ρ still shows semiconducting temperature dependence but the change is more gradual with a noticeable shoulder around 10 K. Most importantly, the Seebeck coefficient is positive (with the exception of the 60 min sample above 175 K). This marked difference from standard chalcopyrite behavior leads us to believe that impurities are responsible for the observed electrical properties of the samples. While chalcopyrite makes up the bulk of the grains as confirmed by XRD, the composition of their surface remains uncertain and may be changed during hot pressing and high temperature transport experiments. In fact, a thin surface layer covering the grains would evade XRD detection and, if electrically conductive enough, could eclipse the measured electrical properties of the less conductive chalcopyrite phase.

Some of the possible phases with high electrical conductivity and positive Seebeck coefficient from the rich Cu–S, Fe–S and Cu–Fe–S systems are digenite $Cu_{1.8}S$, pyrrhotite $Fe_{1-x}S$ or non-stoichiometric bornite $Cu_{5+x}Fe_{1-x}S_4$.[30]

The XRD analysis of the surface of the hot-press sintered pellets detected bornite Cu_5FeS_4 as another phase in addition to $CuFeS_2$ in the ratio of 2–10 mol%. The concentration exceeding 10% is only limited to the surface of the pellets, as it was revealed by the XRD analysis after removing of several micrometers of the pellet surface which showed $CuFeS_2$ as the only phase in the bulk of the pellets, see the comparison of XRD patterns of the pellet's surface and pulverized pellet in Figure 9. Thin surface of the pellets, if it is electrically conductive enough, could eclipse the measured electrical properties of the less conductive chalcopyrite phase. However, regarding the transport properties of bornite, only the Cu rich phase $Cu_{5+x}Fe_{1-x}S_4$ exhibits reasonable electrical resistivity about $10^{-4}\,\Omega\,m$ and Seebeck coefficient about 100 $\mu V K^{-1}$ which both could explain, considering the high concentration of bornite on the surface of the pellets, the observed low temperature resistivity and Seebeck data.

As noted before, heating the samples above room temperature has an irreversible effect on ρ and S. Upon heating to 600 K, both properties converge around a similar value regardless of sample and can then be cycled fully reversibly between 300 and 600 K. The absolute values and temperature dependence of both ρ and S are then very similar for all the samples. We note that the drift observed upon first heating is a bulk effect as sanding the sides of the samples to remove surface layers had no measurable effect on the properties. Around 450 K, resistivity shows a step and a change of slope. This is better viewed in terms of apparent activation energy E_a calculated from the Arrhenius equation $\rho \sim e^{-Ea/(kT)} = e^{-Eg/(2kT)}$, where k is the Boltzmann constant and E_g is the band gap (see Figure 7B). Above this marked feature, E_a shows little change with temperature and its absolute value corresponds to the band gap of about 0.5 eV. This is consistent with the samples entering intrinsic conduction regime above 500 K. With the increase in conductivity, the chalcopyrite mother phase starts to dominate the observed electrical properties, switching the Seebeck coefficient back to negative values before attaining values of S around $-200\,\mu V K^{-1}$, similar to those observed in low doped chalcopyrite.

Regardless of milling time, all the samples possess very similar values of thermal conductivity in the whole measured temperature range. At room temperature, they are relatively low at about 4 and 5 $W m^{-1} K^{-1}$. At low temperatures, we notice a marked absence of a dielectric peak and κ is one order of magnitude lower than in "standard, high temperature synthesized" chalcopyrite with grain size in the micrometer range. This reduction can be readily attributed to increased phonon scattering due to nanostructuring of the samples. This results from the reduction of grain size and possibly other mechanisms as well, the latter supported by the fact that κ does not follow the standard T^3 dependence. At high temperatures we observe T^{-1} dependence typical for Umklapp phonon scattering. Unlike for ρ and S, thermal conductivity does not change after the samples have been exposed to high temperatures (thermal cycling took several days). This is an important implication for potential thermoelectric applications as there are concerns that heating could lead to grain growth resulting in an increase of κ. Let us note that this study focused on stoichiometric $CuFeS_2$ and not on the optimization of thermoelectric properties with respect to TE application and high TE performance. This would require optimized doping by an introduction of doping elements. For the sake of completeness, we note that the values of the thermoelectric figure of merit $ZT = S^2T/(\rho\kappa)$ was about 0.1 and in the case of power factor $PF = S^2/\rho$ of the order of $10^{-5}\,W m^{-1} K^{-2}$ at most for all tested samples.

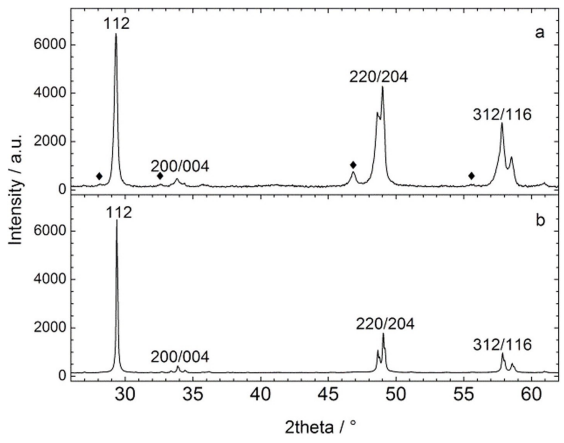

Figure 9. Powder X-ray diffraction patterns of hot-press sintered pellets of chalcopyrite $CuFeS_2$, milling time 180 min. ◆ Cu_5FeS_4 Impurity. a) surface of the pellet, b) pulverized pellet.

3. Conclusions

In this work chalcopyrite $CuFeS_2$ phases were synthesized from elemental precursors via environmentally friendly and essentially waste-free mechanochemical process in a planetary mill. The prolonged milling was applied to identify the physicochemical changes of the synthesized samples. The methods of XRD, SEM, EDX and UV/Vis, adsorption measurements and tests of chemical reactivity were used to examine both powders and sintered ceramics. The X-ray diffractometry patterns of milled powder samples revealed the nanocrystalline and disordered structure of synthetized powders: the crystallite sizes 13, 9, 14 and 13 nm and the strain 16, 14, 17 and 22 were calculated for $CuFeS_2$ milled for 60, 120, 180 and 240 min, respectively. The parameter S_{BET}/X (S_{BET} – specific surface area, X – crystallinity) defined as the structure sensitivity was introduced to completely characterize surface and bulk changes in the treated powder samples. The structure sensitivities of the rate constant of leaching, k as well as the band gap, E_g illustrate the universal character of this parameter for characterization of mechanically activated solids in general (semiconductor physics, chemical

engineering and so on). Here the sulfur liberation during milling leads to the rupture of chemical bonds in which the sulfur is involved and, subsequently, to the reconstruction of chalcopyrite structure. Mechanical impact may lead to the delocalization of copper ions in chalcopyrite sublattice while such liquid-like state of copper is beneficial for acceleration of its chemical leaching (nano-powders) as well as for lowering the thermal conductivity (sintered nano-ceramics).

Thermoelectric measurements on sintered samples did not show any clear and evident correlation with milling time. Electrical resistivity and Seebeck coefficient measurements showed the samples were semiconducting. The measured values were affected by a small concentration of impurities such as bornite – at high temperatures, these values were as expected for chalcopyrite, while at medium temperatures, impurities caused switching of Seebeck coefficient to positive values along with reduced resistivity lowered at low temperatures. Thermal conductivity was very similar in all the samples, nanostructuration resulted in its low values along with suppression of the dielectric peak and, most importantly, thermal cycling targeted to assess long term stability did not have any effect neither on absolute value nor on the temperature dependence.

Experimental Section

Materials

For mechanochemical synthesis of chalcopyrite $CuFeS_2$ copper (99% Merck, Germany), iron (99% Aldrich, Germany), and sulfur (99% CG-Chemikalien, Germany) as reaction precursors were used.

Mineral chalcopyrite $CuFeS_2$ (deposit Slovinky, Slovakia) obtained by sieving on a sieve with mesh size below 35 μm was applied as a standard reference (non-activated) sample for determination of the crystalline phase content in synthesized chalcopyrites. The mineral contains small amounts of quartz SiO_2 and siderite $FeCO_3$ as natural admixtures present in the mineral deposit.

Mechanochemical Synthesis

Mechanochemical synthesis was performed in a laboratory planetary ball mill Pulverisette 6 (Fritsch, Germany) working under the following conditions: 250 mL tungsten carbide milling chamber, tungsten carbide balls with diameter 10 mm and total mass 360 g, revolutions of the mill 550 min^{-1}, milling times 60–240 min, argon atmosphere, the total feed of reaction precursors applied in a stoichiometric ratio 5 g per batch.

Characterization Techniques

X-Ray Diffractometry (XRD)

For the determination of chalcopyrite the XRD patterns were collected again using a D8 Advance diffractometer (Brucker, Germany) with the $Cu_{K\alpha}$ radiation in the Bragg-Brentano configuration. The generator was set up at 40 kV and 40 mA. The divergence and receiving slits were 0.3° and 0.1 mm, respectively. The XRD patterns were recorded in the range of 20–65° 2θ with a step of 0.05°. The XRD line broadening was analyzed by the refinement of regular Thompson-Cox-Hastings pseudo-Voigt function parameters. In order to obtain proper geometry set-up and to eliminate instrumental broadening the instrumental resolution function was determined by refinement of LaB6 standard specimen. The JCPDS PDF database was utilized for phase identification.

For determination of the crystalline phase content of $CuFeS_2$ the relative method put forward by Ohlberg and Strickler was used.[31] The effect of mechanical activation can be evaluated by a mass fraction of the crystalline phase in the activated sample (crystallinity degree), X compared with the reference substance (non-activated) which is assumed to correspond to 100% crystallinity. Thus it holds that

$$X = (I_x/U_x) : (I_o/U_o) \cdot 100\,(\%) \quad (1)$$

where U_o and U_x denote the backgrounds of non-activated (reference) and activated sample while I_o and I_x are integral intensities of diffraction lines of non-activated (reference) and activated samples, respectively.

Scanning Electron Microscopy (SEM)

The morphology and size of the powder particles were investigated by using a scanning electron microscope (SEM) Tescan Vega 3 LMU (Tescan, Czech Republic) using accelerating voltage 20 kV. In order for samples to be conductive, the powder was covered by a layer of gold on fine coat ion sputter JFC 1100. To obtain the information about chemical composition of particles, the energy dispersive X-ray spectrometer (EDX) Tescan: Bruker XFlash Detector 410M (Bruker, Germany) was used.

Specific Surface Area (S_{BET}) Measurements

A nitrogen-adsorption apparatus NOVA 1200e Surface Area & Pore Size Analyzer (Quantachrome Instruments, Great Britain) was employed to record the nitrogen adsorption-desorption isotherms at the temperature of liquid nitrogen. The specific surface area (S_{BET}) values were calculated using the Brunauer-Emmett-Teller (BET) equation.

UV/Vis Spectroscopy

UV/Vis spectra were collected using the UV/Vis spectrophotometer Helios Gamma (Thermo Electron Corporation, Great Britain) at room temperature in a quartz cell by dispersing of synthesized particles in absolute ethanol by ultrasonic stirring for 5 min. The optical band gap was estimated by plotting $(\alpha h\nu)^2$ as a function of the photon energy hν. Extrapolating the straight line portion of the Tauc plot for zero absorption coefficient ($\alpha = 0$) gives the optical band gap energy.

Leaching Experiments

To evaluate a bonding strength of copper and iron in $CuFeS_2$ structure the acid leaching tests were performed. For solubilization of both metals hydrochloric acid HCl was used. Cu and Fe is released into acid solution in the absence of oxygen according to the equation[32]

$$CuFeS_2 + 4\ HCl \rightarrow CuCl_2 + FeCl_2 + 2H_2S \quad (2)$$

The leaching was investigated in a 500 mL glass reactor where 250 mL of HCl solution (10%) was placed. The revolutions of stirrer

was 400 min^{-1}. After heating of the reactor to temperature 343 K, 500 mg of $CuFeS_2$ was added for starting the dissolution of Cu and Fe into the solution. Aliquots (1 mL) of the solution were withdrawn at appropriate time intervals (1, 2, 5, 10, 15, 20, 30, 45, and 60 min) for determination of the concentration of dissolved metals by atomic absorption spectroscopy.

Thermoelectric Measurements

In order to allow thermoelectric characterization, the powders were hot pressed into pellets 12 mm in diameter and about 2 mm thick at 773 K and 50 MPa for 1 h. The pellets were then cut into smaller samples for different measurements. The low-temperature (2–300 K) measurements of the electrical resistivity ρ, thermoelectric power S and thermal conductivity κ were performed with a home-made apparatus (the 60 min sample) or with the Physical Property Measurement System (PPMS) by Quantum Design (all other samples). Both instruments employ the thermal and electrical four-probe method. The measurements were realized on bar-shaped (ca. $2\times2\times10$ mm^3) samples with silver leads attached with a small amount of conductive nickel paste. The high temperature (300–600 K) measurements of the electrical resistivity ρ and thermoelectric power S were performed in dynamic nitrogen atmosphere with a home-made instrument employing the four-probe method with S-type miniature thermocouples, used simultaneously as electrical leads, and mechanically pressed onto the bar-shaped sample, (ca. $2\times2\times6$ mm^3). The thermal diffusivity D and heat capacity Cp was measured using light flash analysis (LFA) in a nitrogen atmosphere from 173 to 573 K on graphite-coated square-shaped samples (ca. $6\times6\times1$ mm^3) using the Netzsch LFA 467 instrument. Pyroceram was used as the heat-capacity standard and the thermal conductivity κ was subsequently calculated by employing the relation $\kappa = D.C_p \cdot \rho$, where ρ is the experimental density.

Acknowledgements

This work was promoted by the Slovak Research and Development Agency under contract No. APVV-18-0357. The support through the Slovak Grant Agency VEGA (project 2/0044/18) is also thankfully acknowledged. Further support was provided by Czech Science Foundation, project 18-12761S, the program of Czech Research Infrastructures, project no. LM2018096, and by MEYS, project No. SOLID21 – CZ.02.1.01/0.0/0.0/16_019/0000760).

Conflict of Interest

The authors declare no conflict of interest.

Keywords: chalcopyrite · energy materials · mechanochemistry · semiconductors · thermoelectrics

[1] F. Habashi, *Chalcopyrite its Chemistry and Metallurgy*, McGraw-Hill, New York **1978**, p. 165.
[2] a) T. E. Engin, A. V. Powell, S. Hull, *J. Solid State Chem.* **2011**, *184*, 2272–2277; b) A. V. Powell, *J. Appl. Phys.* **2019**, *126*; c) T. Wen, Y. G. Wang, N. N. Li, Q. Zhang, Y. S. Zhao, W. E. Yang, Y. S. Zhao, H. K. Mao, *J. Am. Chem. Soc.* **2019**, *141*, 505–510.
[3] Y. L. Li, T. S. Zhang, Y. T. Qin, T. Day, G. J. Snyder, X. Shi, L. D. Chen, *J. Appl. Phys.* **2014**, *116*, 203705.
[4] T. Teranishi, *J. Phys. Soc. Jpn.* **1961**, *16*, 1881–1887.
[5] a) P. Vaqueiro, A. V. Powell, *J. Mater. Chem.* **2010**, *20*, 10950–10950; b) K. Suekuni, T. Takabatake, *APL Mater.* **2016**, *4*, 104503; c) S. Hebert, D. Berthebaud, R. Daou, Y. Breard, D. Pelloquin, E. Guilmeau, F. Gascoin, O. Lebedev, A. Maignan, *J. Phys. Condens. Matter* **2016**, *28*, 013001.
[6] a) R. Ang, A. U. Khan, N. Tsujii, K. Takai, R. Nakamura, T. Mori, *Angew. Chem. Int. Ed.* **2015**, *54*, 12909–12913; *Angew. Chem.* **2015**, *127*, 13101–13105; b) P. Balaz, E. Dutkova, P. Levinsky, N. Daneu, L. Kubickova, K. Knizek, M. Balaz, J. Navratil, J. Kasparova, V. Ksenofontov, A. Moller, J. Hejtmanek, *Mater. Lett.* **2020**, *275*, 128107.
[7] a) N. Tsujii, *J. Electron. Mater.* **2013**, *42*, 1974–1977; b) N. Tsujii, T. Mori, *Appl. Phys. Express* **2013**, *6*; 043001; c) N. Tsujii, T. Mori, Y. Isoda, *J. Electron. Mater.* **2014**, *43*, 2371–2375; d) N. Tsujii, F. Q. Meng, K. Tsuchiya, S. Maruyama, T. Mori, *J. Electron. Mater.* **2016**, *45*, 1642–1647; e) D. Berthebaud, O. I. Lebedev, A. Maignan, *J. Mater.* **2015**, *1*, 68–74; f) R. Lefevre, D. Berthebaud, M. Y. Mychinko, O. I. Lebedev, T. Mori, F. Gascoin, A. Maignan, *RSC Adv.* **2016**, *6*, 55117–55124; g) H. Y. Xie, X. L. Su, Y. G. Yan, W. Liu, L. J. Chen, J. F. Fu, J. H. Yang, C. Uher, X. F. Tang, *NPG Asia Mater.* **2017**, *9*, e390; h) L. Vaure, Y. Liu, D. Cadavid, F. Agnese, D. Aldakov, S. Pouget, A. Cabotu, P. Reiss, P. Chenevier, *ChemNanoMat* **2018**, *4*, 982–991; i) J. Navratil, J. Kasparova, T. Plechacek, L. Benes, Z. Olmrova-Zmrhalova, V. Kucek, C. Drasar, *J. Electron. Mater.* **2019**, *48*, 1795–1804.
[8] a) L. D. Hicks, M. S. Dresselhaus, *Phys. Rev. B* **1993**, *47*, 16631–16634; b) L. D. Hicks, M. S. Dresselhaus, *Phys. Rev. B* **1993**, *47*, 12727–12731; c) M. S. Dresselhaus, G. Chen, M. Y. Tang, R. G. Yang, H. Lee, D. Z. Wang, Z. F. Ren, J. P. Fleurial, P. Gogna, *Adv. Mater.* **2007**, *19*, 1043–1053; d) K. Biswas, J. Q. He, I. D. Blum, C. I. Wu, T. P. Hogan, D. N. Seidman, V. P. Dravid, M. G. Kanatzidis, *Nature* **2012**, *489*, 414–418; e) J. P. Heremans, M. S. Dresselhaus, L. E. Bell, D. T. Morelli, *Nat. Nanotechnol.* **2013**, *8*, 471–473; f) J. Q. He, M. G. Kanatzidis, V. P. Dravid, *Mater. Today* **2013**, *16*, 166–176.
[9] a) P. F. P. Poudeu, J. D'Angelo, A. D. Downey, J. L. Short, T. P. Hogan, M. G. Kanatzidis, *Angew. Chem. Int. Ed.* **2006**, *45*, 3835–3839; *Angew. Chem.* **2006**, *118*, 3919–3923; b) S. Johnsen, J. Q. He, J. Androulakis, V. P. Dravid, I. Todorov, D. Y. Chung, M. G. Kanatzidis, *J. Am. Chem. Soc.* **2011**, *133*, 3460–3470.
[10] a) D. X. Liang, R. S. Ma, S. H. Jiao, G. S. Pang, S. H. Feng, *Nanoscale* **2012**, *4*, 6265–6268; b) J. Park, Y. Xia, V. Ozolins, *J. Appl. Phys.* **2019**, *125*, 125102.
[11] a) P. Balaz, *Mechanochemistry in Nanoscience and Minerals Engineering*, Springer, Berlin Heidelberg, **2008**, p. 413; b) P. Balaz, M. Balaz, M. Achimovicova, Z. Bujinakova, E. Dutkova, *J. Mater. Sci.* **2017**, *52*, 11851–11890.
[12] Y. C. Lan, A. J. Minnich, G. Chen, Z. F. Ren, *Adv. Funct. Mater.* **2010**, *20*, 357–376.
[13] E. Dutkova, Z. Bujnakova, J. Kovac, I. Skorvanek, M. J. Sayagues, A. Zorkovska, J. Kovac, P. Balaz, *Adv. Powder Technol.* **2018**, *29*, 1820–1826.
[14] P. Levinsky, J. Hejtmanek, K. Knizek, M. Pashchenko, J. Navratil, P. Masschelein, E. Dutkova, P. Balaz, *Acta Phys. Pol. A* **2020**, *137*, 904–907.
[15] P. Balaz, M. Achimovicova, M. Balaz, K. Chen, O. Dobrozhan, E. Guilmeau, J. Hejtmanek, K. Knizek, L. Kubickova, P. Levinsky, V. Puchy, M. J. Reece, P. Varga, R. Zhang, *ACS Sustainable Chem. Eng.* **2021**, *9*, 5, 2003–2016.
[16] a) S. X. Zhao, G. R. Wang, H. Y. Yang, G. B. Chen, X. M. Qiu, *Trans. Nonferrous Met. Soc. China* **2021**, *31*, 1465–1474; b) D. B. Cullity, *Elements of X-ray Diffraction*, Second Edition, Addison-Wesley Publishing Company, Inc., London, **1978**.
[17] A. Z. Juhasz, L. Opoczky, *Mechanical Activation of Minerals by Grinding: Pulverizing and Morphology of Particles*, Ellis Horwood, Chichester, **1990**, p. 213.
[18] K. Tkacova, *Mechanical Activation of Minerals*, Elsevier, Amsterdam **1989**, p. 155.
[19] V. V. Boldyrev, K. Tkacova, *J. Mater. Synth. Process.* **2000**, *8*, 121–132.
[20] a) K. Miyasaka, M. Senna, *React. Solids* **1986**, *2*, 135–149; b) S. I. Inoue, M. Senna, *React. Solids* **1988**, *5*, 155–166.
[21] M. Senna, *Part. Part. Syst. Charact.* **1989**, *6*, 163–167.
[22] K. Tkacova, P. Balaz, *Hydrometallurgy* **1988**, *21*, 103–112.
[23] W. G. Zeier, A. Zevalkink, Z. M. Gibbs, G. Hautier, M. G. Kanatzidis, G. J. Snyder, *Angew. Chem. Int. Ed.* **2016**, *55*, 6826–6841; *Angew. Chem.* **2016**, *128*, 6938–6954.
[24] Z. T. Tian, K. Esfarjani, J. Shiomi, A. S. Henry, G. Chen, *Appl. Phys. Lett.* **2011**, *99*, 053122.
[25] a) P. Balaz, Z. Bastl, K. Tkacova, *J. Mater. Sci. Lett.* **1993**, *12*, 511–512; b) J. H. Li, Q. Tan, J. F. Li, *J. Alloys Compd.* **2013**, *551*, 143–149; c) G.

Granata, K. Takahashi, T. Kato, C. Tokoro, *Miner. Eng.* **2019**, *131*, 280–285; d) Z. W. Huang, L. D. Zhao, *J. Mater. Chem. C* **2020**, *8*, 12054–12061.
[26] a) P. Balaz, K. Tkacova, E. G. Avvakumov, *J. Therm. Anal.* **1989**, *35*, 1325–1330; b) E. Gock, *Erzmetall* **1978**, *31*, 282–288 (in German).
[27] K. Tkacova, V. V. Boldyrev, Yu. T. Pavluchin, E. G. Avvakumov, R. Sch. Sadykov, P. Balaz, *Izv. Sib. Otdel. AN SSSR 2* **1984**, 9–13 (in Russian).
[28] P. Baláž, *Extractive Metallurgy of Activated Minerals*, Elsevier, Amsterdam **2000**, p. 278.
[29] J. Navratil, P. Levinský, J. Hejtmánek, M. Pashchenko, K. Knizek, L. Kubickova, T. Kmjec, C. Drasar, *J. Phys. Chem. C* **2020**, *124*, 20773–20783.
[30] a) Z. H. Ge, B. P. Zhang, Y. X. Chen, Z. X. Yu, Y. Liu, J. F. Li, *Chem. Commun.* **2011**, *47*, 12697–12699; b) C. I. Pearce, R. A. D. Pattrick, D. J. Vaughan, *Rev. Mineral. Geochem.* **2006**, *61*, 127–180; c) P. Qiu, T. Zhang, Y. Qiu, X. Shi, L. Chen, *Energy Environ. Sci.* **2014**, *7*, 4000–4006.
[31] S. M. Ohlberg, D. W. Strickler, *J. Am. Ceram. Soc.* **1962**, *45*, 170–171.
[32] Y. Li, N. Kawashima, J. Li, A. P. Chandra, A. R. Gerson, *Adv. Colloid Interface Sci.* **2013**, *197–198*, 1–32.

Manuscript received: June 16, 2021
Revised manuscript received: June 23, 2021